

Northumbria Research Link

Citation: Lu, Jinwen, Yang, Xirong, Zhao, Yongqing, Dong, Longlong, Fu, Richard, Du, Yan, Zhang, Wei and Zhang, Yusheng (2019) Influence of α s precipitates on electrochemical performance and mechanical degradation of Ti-1300 alloy. Journal of Alloys and Compounds, 803. pp. 88-101. ISSN 0925-8388

Published by: Elsevier

URL: <https://doi.org/10.1016/j.jallcom.2019.06.266>
<<https://doi.org/10.1016/j.jallcom.2019.06.266>>

This version was downloaded from Northumbria Research Link:
<http://nrl.northumbria.ac.uk/id/eprint/39871/>

Northumbria University has developed Northumbria Research Link (NRL) to enable users to access the University's research output. Copyright © and moral rights for items on NRL are retained by the individual author(s) and/or other copyright owners. Single copies of full items can be reproduced, displayed or performed, and given to third parties in any format or medium for personal research or study, educational, or not-for-profit purposes without prior permission or charge, provided the authors, title and full bibliographic details are given, as well as a hyperlink and/or URL to the original metadata page. The content must not be changed in any way. Full items must not be sold commercially in any format or medium without formal permission of the copyright holder. The full policy is available online: <http://nrl.northumbria.ac.uk/policies.html>

This document may differ from the final, published version of the research and has been made available online in accordance with publisher policies. To read and/or cite from the published version of the research, please visit the publisher's website (a subscription may be required.)

Influence of α_s precipitates on electrochemical performance and mechanical degradation of Ti-1300 alloy

Jinwen Lu ^{a*}, Xirong Yang ^b, Yongqing Zhao ^{a*}, Longlong Dong ^a, Yongqing Fu ^c, Yan Du ^a, Wei Zhang ^a,
Yusheng Zhang ^a

^a Advanced Materials Research Central, Northwest Institute for Nonferrous Metal Research, Xi'an 710016, China

^b School of metallurgical Engineering, Xi'an University of Architecture and Technology, Xi'an 710055, China

^c Faculty of Engineering and Environment, Northumbria University, Newcastle upon Tyne NE1 8ST, UK

Abstract: The influence of α_s precipitates on electrochemical behavior and mechanical degradation of Ti-1300 alloy in artificial seawater have been studied. The results show that corrosion resistance and mechanical degradation have been significantly affected by the formation of acicular α_s precipitates. The precipitated α_s phase with an acicular shape around 40 ~ 60 nm in width are uniformly distributed inside β grain. Many α_s precipitates are intersected each other and keep a well-defined Burgers orientation relationship with β matrix, which restricts the growth of other α_s phases due to pinning effect. Within the electrolyte, the α_s phases can form “microgalvanic cells” with their adjacent intergranular β phases, which dramatically deteriorate its corrosion resistance. The mechanical properties of the alloy are also degraded with the increase of immersion time due to the pitting reaction. The precipitated microstructure exhibits an inferior mechanical degradation behavior, and this is mainly because a lot of corrosion cavities are nucleate d and propagated at the interface between α_s precipitates and prior β grains.

Keywords: Titanium, Passive film, Pitting corrosion, Mechanical degradation performance

1. Introduction

Owing to their high specific strength, excellent workability, and outstanding corrosion

* E-mail address: lujwen@163.com(Jinwen Lu), trc@c-nin.com (Yongqing Zhao)

1 resistance, metastable β titanium (Ti) alloys have been extensively used in aeronautics,
2 petrochemical and nuclear industry [1-3]. It is well known that titanium and its alloys can rapidly
3 react with oxygen molecules in electrolyte and form a protective oxide layer with a thickness of
4 several nanometer [4-6], which provides a good corrosion resistance. Comparing with α or $\alpha+\beta$ Ti
5 alloys, β Ti alloys not only have excellent mechanical properties due to the precipitation of
6 primary/secondary α phases (e.g., α_p and α_s) after thermomechanical processing, but also improves
7 corrosion resistance due to the formation of the massive β elements oxides [7]. The service life of
8 β Ti alloys is dependent on their corrosion behavior, and it was reported that their metallurgical
9 defects and different service environments (such as those in chemical and marine industries) cause
10 various types of corrosion damages [8, 9]. According to literature [10-12], the formed passive
11 protective layer can be gradually in the electrolyte due to the concentrated corrosive ions (such as
12 F^- and Cl^-), and pitting corrosion appears after the oxide layer is destroyed [8, 13]. This process
13 can be explained by the preferred adsorption of corrosive ions [9]. Excessive metallic ions
14 released by leaching or synergetic effects of corrosion reaction and mechanical loading, can
15 significantly increase stress corrosion fracture and decrease the fatigue strength of the alloy.
16 Therefore, it is critical to find a way to improve the corrosion resistance for Ti alloy.

17 It is well known that corrosion resistance and passivation behavior of Ti alloys are relied on
18 the microstructures and relative density of passive layer [13, 14]. Some studies [15-17] reported
19 that the passive film formed on Ti alloy surface is mainly composed of titanium oxide (TiO_2), and
20 also a small amount of suboxides (TiO and Ti_2O_3). This passive film exhibits a bi-layer structure,
21 e.g., an inner barrier layer at the metal/oxide interface and an outer porous layer at the
22 solution/oxide interface, and the stability of passive film is dominated by the inner barrier layer

1 [14, 17, 18]. In addition, some researchers have also investigated corrosion behavior of Ti alloys
2 with the addition of different alloying elements [16-20]. It is found that two types of alloying
3 elements can effectively inhibit local breakdown or dissolution of passive film. The first type is
4 cathodic alloying elements [19, 20], with their representative elements of platinum-group metals
5 (such as Pd, Pt, Ni and Ru). The enhancement of corrosion resistance is mainly due to the
6 acceleration of cathodic reactions, which can change the corrosion potential to a critical value in
7 passive region, thus resulting in lower passive current densities and improving passivity [10]. The
8 second type is anodic alloying elements, which can reduce thermodynamic instability and anodic
9 activity of Ti alloy [18, 21, 22]. The representative elements are Mo, Ta, Zr, V, Cr, Nb, etc [5, 23,
10 24]. Li [15], Bai [18] and Yu [25] reported the effects of Zr, Nb, Mo and Ta alloying on corrosion
11 properties of Ti alloys. It was reported that passive film is composed of several different oxides,
12 including TiO₂, Nb₂O₅, ZrO₂, MoO₂ and Ta₂O₅ [9]. These oxides can enhance the integrity and
13 the stability of the passive film, thus improving the resistance of titanium alloys due to the
14 formation of a strong covalent bond with neighboring Ti, Zr, Ta and Nb atoms through sharing of
15 d level electrons [9].

16 In addition, the microstructure is also a key factor to influence the corrosion performance of β
17 Ti alloys [13]. Some studies showed that the $\alpha+\beta$ interphase acted as a preferential dissolution
18 locations to trigger the pitting reaction [5, 13]. However, there are still a lot of unsolved problems
19 for improving the corrosion performance of Ti alloy. For example, in oxidizing environments such
20 as nitric acid solutions, Ti alloy can spontaneously form a compact passive film, which protects
21 the matrix [26, 27]. By contrast, in reducing environments such as hydrochloric acids, Ti alloys
22 present relatively poorer corrosion resistance due to the influence of corrosive ions (such as F⁻ and

Cl⁻) on the anodic process [11, 19, 28, 29].

In the present work, the effects of nano-precipitates of α_s phase on passive behavior and corrosion performance of Ti-1300 alloy is studied in artificial seawater with different pH values, and the degradation of mechanical properties after different immersion times is also investigated by using tensile testing method with a slow strain rate. The corrosion mechanism is discussed based on surface analysis and microstructural characterization.

2. Experimental

2.1 Material

Ti-1300 alloy used in this study was fabricated by vacuum consumable arc-remelting furnace under an argon protection atmosphere. The ingots were re-melted three times to ensure chemical homogeneity. They were then hot forged at 950 °C into square-shaped billets with 50mm in all dimensions. Finally, the circular rods with a diameter of 11 mm were obtained by hot rolling at 750 °C. Compositional optimization was performed using First-principles calculations in Ti-Al-X system with β -stabilizing elements in order to achieve superior mechanical properties. The chemical composition was tested as following (in wt. %): 5.15 Al, 2.96 Zr, 3.96 Cr, 3.79 Mo and 3.95 V with the balance Ti, as measured by Inductively coupled plasma massspectrometry (ICP-MS). The α/β phase transition temperature determined by the standard metallographic method was approximately 830 °C. The details of quantitative metallography are as follows: cylindrical specimens (Φ 11 mm \times 10 mm) were cut from circular bars and were solution treated at various temperatures, both above and below the α/β phase transition temperature and examined metallographically. The specimens were solution-treated in the temperature range of 800 - 860 °C for 1 hour in an electric furnace and then water quenched to examine the microstructure

(metallographic techniques). The α/β phase transition temperature was identified from the cross-section microstructure analysis. When the solution temperature was above 830 °C, the microstructure was a pure β phase. Therefore, the α/β phase transition temperature of the alloy was identified to be 830 ± 5 °C. The equiaxed microstructure was obtained by solution treated at 870 °C for 1h and air cooling, and the precipitated microstructure was achieved by the single β phase solution and aging treatment (treated at 500 °C for 6 hours and air cooled at ambient temperature).

2.2 Microstructural characterization

Microstructural characterization was performed using an optical microscope (OM, Leica MPS 30), scanning electron microscope (SEM, JSM-6700, Japan) and transmission electron microscope (TEM, JEOL, JEM-2100). The specimens for OM and SEM were polished using the 2000 grid SiC paper, then etched in a Kroll's reagent (1 vol. % HF, 3 vol. % HNO₃, and 5 vol. % H₂O), and ultrasonically cleaned in ethanol and distilled water in sequence. The thin TEM foils were electropolished using a twin-jet technique in a solution of 10 % perchloric acid and 90 % methanol at a voltage of 30 V and a temperature of -35 °C. Crystalline phase analysis was performed using by X-ray diffraction (XRD) analysis with Cu-K α radiation source operated at 30 kV and 300 mA (XRD, D8, ADVANCE). The microstructural analysis (such as volume fraction, grain size and length-width ratio) of α_s precipitates was carried out by using the image analysis software of Image J. To investigate the compositions of the passive films and chemical states of the alloying elements, X-ray photoelectron spectroscopy (XPS) analysis was performed on the film after its immersion in the artificial seawater solutions for 24 hours.

2.3 Electrochemical measurements

1 Electrochemical measurements were carried out with an IM6 Zahner-electrik GmbH
2 (Zenniom, Germany) electrochemical workstation. A conventional three-electrode system was
3 adopted using a saturated calomel electrode (SCE) as the reference electrode and a platinum plate
4 (15mm×15mm) as the counter electrode, and the measured sample with a certain exposed area
5 (0.95 cm²) as the working electrode. Artificial seawater solutions with different pH value were
6 used as electrolyte, and their compositions are listed in Table 1 [30]. The pH value in the
7 electrolyte was adjusted by adding different HCl (1 M) or NaOH (1 M) solutions. Prior to the
8 electrochemical tests, the samples were immersed in the electrolyte to obtain a stable corrosion
9 potential. Open circuit potential (OCP) measurement was conducted for 60 min, which started
10 from the moment when the electrode was immersed into the electrolyte. Potentiodynamic
11 polarization (PP) tests were performed in the range from -1 V to 2 V at a scan rate of 0.5 mV/s.
12 Electrochemical impedance spectroscopy (EIS) measurements were carried out under the
13 potentiostatic condition at OCP with a 10 mV amplitude AC voltage signal, and the applied
14 frequency range was from 10⁵ Hz down to 10⁻¹ Hz. The obtained EIS spectra were fitted using the
15 Zsimpwin software. Each test was performed three times with a fresh solution and a new specimen
16 at 25°C± 0.5 °C.

17 2.4 Immersion tests

18 Immersion tests were performed in a 5 M HCl solution at 25 °C. The specimens (Φ11 mm ×
19 5 mm) were cut and ground using 2000 grit SiC paper, and then cleaned ultrasonically with
20 acetone and deionized water. This cleaning protocol was same for the electrochemical samples.
21 During immersion tests, the specimens were immersed in 450 ml HCl solutions under the ambient
22 environment, and the solution was removed every 2 days over a 10 days immersion period. In

1 order to verify the validity of immersion result, immersion test of each sample was repeated twice,
2 and the experimental data was accordingly obtained from the average of two immersion results.
3 The morphology of the corroded surface after different immersion periods was examined using
4 SEM (JSM-6700, Japan).

5 **2.5 Mechanical tests**

6 Mechanical properties of Ti-1300 alloy were studied using a slow strain rate testing (SSRT)
7 method in 5 M HCl solution at 25 °C. The standard cylindrical tensile specimen with a gage length
8 of 25 mm and a cross section diameter of 5 mm was used in this study, and a strain rate of 1×10^{-5}
9 mm/s was applied until the fracture of the sample. In order to confirm the validity of tensile test
10 results, tests of each condition was repeated twice, and the ultimate tensile strength, yield strength,
11 and elongation were obtained from the average of two tensile results. After the tensile test, the
12 fracture surface was cleaned ultra-sonically, and then observed using SEM (JSM-6460, Japan) to
13 identify the fracture mode.

14 **3. Results and discussion**

15 **3.1 Microstructural characterization**

16 Fig. 1(a) shows XRD results of Ti-1300 alloys with different microstructures, which show
17 that the phase composition for precipitated microstructure is consisted of α and β phases, but only
18 β phase can be detected for equiaxed microstructure. The clear evidence for the phase variations is
19 the differences of the reflection peak near $2\theta = 40.5^\circ$ for α_s phase, which has the same crystal
20 structure with α phase. In addition, the (110) peak of β phase (near $2\theta = 38.5^\circ$) is broadened and
21 its intensity becomes weakening with the precipitation of α_s phase. This phenomenon clearly
22 indicates that the volume fraction of β phase decreases with the precipitation of α_s phase [31].

1 Fig. 1(b) and Fig. 1(c) show the OM micrographs of Ti-1300 alloy with equiaxed and
2 precipitated microstructures, and the higher magnified SEM image for precipitated microstructure
3 is given in Fig. 1(d). It shows the equiaxed β grains with an average grain size of approximately
4 $73.05\ \mu\text{m}$ (Fig. 1(b)). This microstructure is typical character for Ti alloys within the single β
5 region (e.g., above α/β phase transition temperature), which means that the recrystallization of the
6 deformed grains has fully completed [32]. As can be seen from Fig. 1(c), the precipitated
7 microstructure consists of acicular α_s precipitates and intergranular β phase. Moreover, the prior β
8 grain boundaries are straight and clear, and the primary β grain size is around $87.82\ \mu\text{m}$, indicating
9 that the recrystallization for prior β grain occurred [32]. As shown in Fig. 1(d), the acicular shape
10 α_s phases around $40 \sim 60\ \text{nm}$ in width are uniformly distributed into prior β grain, and their
11 average volume fraction and length-width ratio are 19.50 % and 13.11, respectively.

12 Fig. 2 shows bright and dark field TEM micrographs of the acicular α_s precipitates, inset
13 shows their corresponding diffraction pattern. Fig. 2(a) shows that the precipitated microstructure
14 consists of acicular α_s platelets uniformly distributed inside the β phase matrix, and selective area
15 diffraction (SAD) patterns confirm the presence of α_s platelets. Acicular α_s phases (bright fine
16 acicular shape) are homogeneously precipitated in β matrix (darker contrast), and which can be
17 seen from the dark-field micrograph as shown in Fig. 2(b). Many α_s platelets mutually intersect
18 each other, and the other precipitates within β matrix along a specific habit plane, which restricts
19 the mobility of prior β grain boundaries and the growth of other α_s phase due to the significant
20 pinning effect. Moreover, the α_s platelets have Burgers orientation relationship with the adjacent β
21 matrix (shown in Fig. S1), and the lath size of the α_s platelets is dependent on the diffusion of
22 atoms cross the boundary during thermal treatment process. This result is consistent with the work

by Chen [33] and Huang [34]. In addition, the precipitated α_s phases are the key strengthening phase for Ti-1300 alloy, which has been reported in our previous work in details [22]. Therefore, precipitation strengthening has been considered to be the main strengthening mechanism for Ti-1300 alloy.

3.2 Electrochemical corrosion behavior

3.2.1 OCP test

Fig. 3(a) and Fig. 3(b) show the OCP results for equiaxed and precipitated microstructures as a function of immersion time in artificial seawater with different pH values. The dependence of the stable OCP on pH value is shown in Fig. 3 (c). When the pH value is lower than 7.5, the OCP evolution curves for both microstructures show a typical passivation characteristic, e.g., the OCP increases rapidly with immersion time in the first 300 s, but then reaching a near-steady-state. These are linked to the spontaneous formation and growth of oxide layers. Referring to *E*-pH diagrams [35], the OCPs fall within the passivation region. Similar phenomenon of spontaneous passivation for β Ti alloys has previously been reported by Nakagawa [19]. When the pH value is increased to 9.54, OCPs for both microstructures decrease rapidly during the initial immersion period (approximately 350 s) and stabilize at relatively lower potentials, which is probably associated with the formation of less stable and non-effectively protective oxide layers [36].

In addition, the OCP for precipitated microstructure in the artificial seawater remains a relatively low steady-state potential when compared with that for the equiaxed microstructure (Fig. 3(c)), implying the generation of an unstable passive layer due to α_s platelets. Previous studies [17, 37] showed that the passive film on Ti surface was mainly composed of TiO_2 and Ti suboxide (such Ti_2O_3 and TiO), TiO_2 was the dominant portion of the outermost layer, the lower oxidation

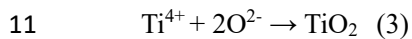
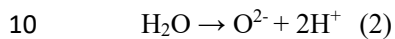
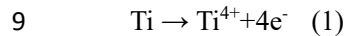
states Ti_2O_3 and TiO were mainly formed at the metal-oxide interface as an inner barrier layer. The OCP was the potential in the stable region of this oxides, and the corrosion resistance was controlled kinetically by the stability of the passive film [9]. For precipitated microstructure, α_s phase acts as the preferential dissolution locations due to the formation of microgalvanic cells between α_s platelets and adjacent intergranular β phase, and the testing results show that α_s phase decreases the stability of the passive film. The similar conclusions have been obtained in the literature [23, 38].

3.2.2 PP measurement

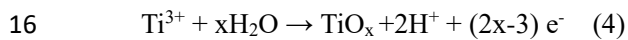
Fig. 4(a) and Fig. 4(b) show the typical PP curves of equiaxed and precipitated microstructures in artificial seawater with different pH value. It is found that electrochemical behaviors for both microstructures based on the polarization curves are similar at each pH value, and the anodic polarization curves do not exhibit a typical active-passive characteristic [9, 15]. When the artificial seawater is in acidic/neutral condition, with the increase of pH values, we found: (i) corrosion potentials (E_{corr}) of both microstructures are shifted towards higher value, (ii) corrosion current density (j_{corr}) decreases to a lower level at the pH value of 7.06 ($1.400 \mu\text{A}/\text{cm}^2$ and $2.430 \mu\text{A}/\text{cm}^2$ for the equiaxed and precipitated microstructures), and (iii) precipitated microstructure under each pH condition presents a much lower E_{corr} and higher j_{corr} in comparing to equiaxed microstructure, especially at the pH value of 1.19 (-0.579 V and $5.870 \mu\text{A}/\text{cm}^2$ for E_{corr} and j_{corr}). This indicates the inferior self-passivating behavior and corrosion resistance of the precipitated microstructure in artificial seawater. Because the electrolyte is under an alkaline condition, the PP curves indicate a much weaker spontaneous passive ability. These results are consistent with those from the OCP tests (Fig. 3(a) and Fig. 3(b)), indicating that the local

1 breakdown or dissolution of passive film has occurred on the surface [14, 15].

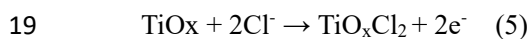
2 It is well known that the change of polarization curves reflects the different corrosion
3 reactions. Cathodic polarization curve shows hydrogen evolution reaction caused by electrolyte
4 reduction, oxygen reduction and the formation of OH groups, whereas anodic polarization
5 presents a typical anodic dissolution reaction and the formation of passive oxide layer [27].
6 According to the literature [27, 35], during the formation of passive layer on Ti alloy surface
7 which does not contain chlorine ions in electrolyte, the transition of ions from metal matrix to the
8 passive reaction interface and the formation of passive film have the following reactions [28, 39]:



12 The reaction between cathodic oxygen and anodic dissolution in the chlorine ions solution is a
13 complex process. It was reported that polarization curve for a non-oxidized Ti sample at low
14 potentials corresponds to the anodic dissolution [9, 10]. Then non-stoichiometric titanium dioxides
15 are generated with a low solubility, which can be expressed using the following reaction [28, 40]:



17 With the further polarization in a positive potential, the formation of unstable titanium oxychloride
18 occurs according to the following reaction [11, 28, 40]:



20 Based on the above corrosion analysis combined with polarization reaction, the formation of
21 passive film on the Ti-1300 surface in the artificial seawater can be divided into three stages. In
22 the first stage, titanium compounds (such as Ti suboxides of Ti_2O_3 and TiO , as well as TiOOH) are

1 formed as insoluble products, and can be adsorbed on the surface of the alloy. In the second stage,
2 titanium oxides are transformed from a less stable Ti_2O_3 into the stable TiO_2 . In the third stage,
3 the oxide layer is thickened with the polarization in the positive direction, and is consisted of Ti
4 dioxide and Ti suboxides (such Ti_2O_3 and TiO).

5 In order to evaluate the corrosion resistance of this spontaneously formed passive system, the
6 different corrosion parameters (such as E_{corr} and j_{corr} as listed in Table 2) were calculated using the
7 Stern-Geary method [28] based on the PD curves. E_{corr} is defined as the potential at which the sign
8 of current is changed during the cathodic to anodic potential sweep, and j_{corr} can be obtained
9 directly by extrapolating the anodic and cathodic Tafel lines to the open-circuit corrosion potential
10 (E_{corr}) [10, 28]. The polarization curves for both microstructures exhibit an obviously passive
11 region, meaning that the formed oxide layer on the surface is stable and protective. Due to the
12 pitting corrosion induced by the concentrated Cl^- ions, the corrosion resistance of both
13 microstructures in the artificial seawater with the pH value of 1.19 is poorer those of the others,
14 and the lowest E_{corr} (-0.579 V) and the highest j_{corr} ($5.870 \mu\text{A}/\text{cm}^2$) are obtained for precipitated
15 microstructure. This is because that the precipitated microstructure is more susceptible to
16 corrosion attack due to the formation of numerous microgalvanic cells, which accelerates pitting
17 process. The different composition of α and β phases causes microgalvanic reactions for Ti-1300
18 alloys, which results in preferential corrosion of α phase and α/β interphase boundaries.

19 3.2.3 EIS measurement

20 Fig. 5(a) and Fig. 5(c) show the Nyquist plots of equiaxed and precipitated microstructures in
21 artificial seawater, while Fig. 4(b) and Fig. 4(d) display Bode plots of the corresponding
22 impedance spectra. Nyquist plots demonstrate that all the samples exhibit a depressed capacitive

1 semicircle with much larger diameter in the high frequency region followed by a straight line in
2 the low frequency region. The capacitive-like semicircle is related to the complete passive barrier
3 layer, and the larger diameters of capacitive semicircles imply that more protective passive films
4 have formed on the surface [8, 41]. As shown in Fig. 5(a) and Fig. 5(c), the capacitive loop shrinks
5 with further increasing of Cl^- ions in the artificial solution, and the radius of the semicircle is
6 substantially decreased. This phenomenon indicates that the charge-transfer resistance becomes
7 less important in the corrosion process with the increase of Cl^- ions [14, 42].

8 As shown in Fig. 5(b) and Fig. 5(d), both the impedance module (Z) and phase angle (θ) of
9 precipitated microstructure are lower than those of equiaxed microstructure, which indicates a
10 weaker electrochemical behavior for the precipitated ones. However, all the absolute impedance
11 curves in a high frequency regime (10^4 - 10^5 Hz) are almost independent of frequency, implying
12 the effect generated from solution resistance (R_s) [19]. With reducing of the frequency, the
13 absolute impedance is firstly increased with a constant slope in the frequency of 10^1 - 10^4 Hz, but
14 with different slope in frequency of 10^{-1} - 10^1 Hz. At the lowest frequency of 10^{-1} Hz, the absolute
15 impedance is reduced with further increases of Cl^- concentration, the corresponding Bode plots in
16 phase angles for both microstructures are also shifted to a value between -75° and -40° , indicating
17 the decreased capacitive influence in the electrochemical behavior of the electrode [43]. The larger
18 diameters of capacitive semicircles and the increased phase angle imply that more protective
19 passive film has formed on the surface of equiaxed microstructure.

20 In general, the impedance response for electrochemical systems reflects a distribution of
21 reactivity that is commonly represented in equivalent electron circuits as a constant-phase element
22 (CPE) [44]. Polarization resistance (R_p) can be used to evaluate the corrosion resistance, which

1 requires to fit the EIS spectra using the equivalent circuit. In this study, the equivalent electron
 2 circuit with one time constants (Fig. 5(e)) is constructed to fit this impedance, which consists of
 3 the parallel combination terms ($R_f Q$) in series with the Ohmic resistance (R_e) [44, 45]. R_e is the
 4 Ohmic resistance and R_f is the charge transfer resistance. The CPE parameters α and Q are
 5 independent of frequency. A CPE was used to improve the fitting quality instead of the ideal
 6 capacitance due to the distribution of relaxation times originating from the surface heterogeneity.
 7 Independent of the cause of CPE behavior, the phase angle associated with a CPE is independent
 8 of frequency. The impedance of CPE (Z_{CPE}) can be expressed as [35]:

$$9 \quad Z_{CPE} = \{Q(j\omega)^\alpha\}^{-1} \quad (6)$$

10 where j is the imaginary number, ω is angular frequency, and α is a factor accounting for the
 11 deviation from the ideal capacitive behavior due to surface in homogeneity, roughness factors and
 12 adsorption effects. When $\alpha = 1$, it is assumed to be an ideal capacitor with the value of Q equals to
 13 the capacitance (C). For $\alpha < 1$, the Q cannot represent the capacitance. Both the Brug formulas and
 14 the Hsu and Mansfeld formula have been widely used to extract effective capacitance values from
 15 CPE parameters for studies on passive films, protective coatings, and corrosion inhibitors [46, 47].
 16 By considering a normal time-constant distribution of the surface layer, Brug et al. proposed Eqs.7
 17 for developing the relationships between interfacial capacitance and CPE parameters for both
 18 blocking and Faradaic systems. The result is demonstrated in Fig. 5(e), where a normal
 19 distribution of time constants results in a distributed time-constant behavior, which can be
 20 expressed as a summation of impedances. The effective capacitance associated with the CPE can
 21 therefore be expressed as [44]:

$$22 \quad C_{eff} = Q^{1/\alpha} (R_e + R_f)^{(1-\alpha)/\alpha} \quad (7)$$

1 For passive alloys in relatively concentrated solutions, $R_f \gg R_e$, Eq. 7 can be simplified to
 2 become Eq. 8.

$$3 \quad C_{\text{eff}} = Q^{1/\alpha} R_f^{(1-\alpha)/\alpha} \quad (8)$$

4 Based on above model, the impedance (Z_ω) of electrode and its polarisation resistance ($R_{\text{p-EIS}}$)
 5 can be calculated using the following expressions [22, 35]:

$$6 \quad Z_\omega = (R_f^{-1} + Q(j\omega)^\alpha)^{-1} \quad (9)$$

7 Polarization resistance ($R_{\text{p-EIS}}$) is given as [35]:

$$8 \quad R_{\text{p-EIS}} = \lim_{\omega \rightarrow 0} (Z_\omega) = R_f \quad (10)$$

9 **Based on** the above equivalent circuits, the calculated impedance parameters **are listed** in
 10 Table 3. Obviously, the good quality of fitting results judged by the quite small chi-square values
 11 suggests the validity of the obtained parameters [36]. The precipitated microstructure has lower
 12 passive film resistance (R_f) and higher capacitance (C_{eff}) than **the** equiaxed microstructure at each
 13 pH, indicating the **formation of** thinner and unstable passive film on the surface. The weakening
 14 corrosion resistance for the precipitated microstructure, which may be contributed to the large
 15 number of **detrimental** microgalvanic cells formed between precipitated α_s and adjacent β phase.
 16 In addition, it is obvious that R_f **is decreased** with the increase of the Cl^- concentration (pH value),
 17 which demonstrates the deterioration effects caused by Cl^- . **However, it is noted** R_f value of the
 18 equiaxed microstructure are always higher than that of precipitated microstructure at each pH
 19 value indicating the superior corrosion resistance, which is in accordance with the results of OCP
 20 measurements and PP tests. $R_{\text{p-EIS}}$ values for precipitated and equiaxed microstructures at various
 21 pH **values** can be obtained by using the Eq (10) from Table 3. $R_{\text{p-EIS}}$ for precipitated microstructure
 22 in seawater solutions with pH **values** of 1.19, 4.22 and 9.54 **are decreased to** 95.68 $\text{k}\Omega \cdot \text{cm}^2$, 120.96

1 $\text{k}\Omega\cdot\text{cm}^2$ and $113.53 \text{ k}\Omega\cdot\text{cm}^2$, respectively, which are two and three times lower than those for the
2 solutions with a pH value of 7.06 ($204.69 \text{ k}\Omega\cdot\text{cm}^2$). It indicates that the passive film becomes
3 much thinner and more porous after adsorption of Cl^- ions, thus results in the deterioration of the
4 corrosion resistance. Cl^- ions not only inhibit the reactivity of the interfacial charge transfer, but
5 also decrease the pitting potential and significantly accelerates the chloride-induced localized
6 corrosion [9, 28, 48, 49]. Therefore, the appearance of α_s phase and corrosive ions (Cl^-) results in
7 the weak corrosion resistance for Ti-1300 alloy in artificial seawater.

8 3.2.4 XPS analysis

9 The alloys subjected to immersion of 24 h in artificial seawater (pH = 7.06), were selected to
10 characterize surface chemical nature of native passive film using XPS. Fig. 6 and Fig. 7 show the
11 high-resolution XPS spectra of Ti 2p, O 1s, Al 2p, Mo 3d, V 2p and Cr 2p recorded at the
12 outermost passive film for both microstructures with different sputtering depths. The native
13 passive films for both microstructures have the same composition, including Ti, Al, Cr and O. The
14 content of Ti increases and that of O rapidly decreases with the increasing sputtering depths, and
15 then becomes equal to each other. According to the peak intensity in high-resolution XPS signals
16 of Ti $2p_{3/2}$, Al $2p_{3/2}$ and Cr $2p_{3/2}$, the main component of passive film is TiO_2 with Ti^{4+} at 459.1 eV,
17 Ti_2O_3 with Ti^{3+} at 457.4 eV, TiO with Ti^{2+} at 455.1 eV, Al_2O_3 with Al^{3+} at 74.3 eV, Cr_2O_3 with Cr^{3+}
18 at 576.9 eV and Cr suboxides with neglectable content with reference to the NIST XPS database
19 [50].

20 The outermost layer is identified as the mixed oxides of TiO_2 , Al_2O_3 and Cr_2O_3 for both
21 microstructures, and these oxides have the highest stability due to thermodynamic reasons [10, 51].
22 With an increasing sputtering depths, the peaks are shifted toward the low binding energy and Ti

1 2p_{3/2} peak is boarder than that of pure TiO₂, suggesting that abundant sub-oxides are present
2 beneath the outer TiO₂ layer. These are mainly Ti₂O₃ and TiO as the oxidation state of Ti is
3 gradually decreased from Ti⁴⁺ through Ti³⁺ and Ti²⁺. When the sputtering time is increased to 60 s,
4 some spectra of Ti 2p_{3/2}, Cr 2p_{3/2} and Al 2p_{3/2} for equiaxed microstructure are still retained, while
5 only some suboxides of Ti and Al are detected for precipitated microstructure. When the sputtering
6 time exceeds 120 s, the spectra of suboxides and Al₂O₃ are detected for equiaxed microstructure,
7 while the precipitated one only exhibits peaks of pure metal elements. The thickness of passive
8 film can be obtained based on the sputtering depths from the XPS spectra. When the sputtering
9 time is given to 1s, the sputtering depth is approximately 0.1 nm for titanium alloy according to
10 the literature [10, 52]. In this study, the film thicknesses for equiaxed and precipitated ones in
11 artificial seawater can be calculated to be 8-10 nm and 4-6 nm, respectively. In precipitated
12 microstructure, the acicular α_s platelets on the β matrix obviously weaken the passivation ability of
13 the alloy due to the potential difference, which induces microgalvanic cells and accelerates pitting
14 reaction [5, 13].

15 3.3 Surface topography characterization

16 Fig. 8 shows the variation of weight loss of precipitated and equiaxed microstructures as a
17 function of immersion time in 5 M HCl solution. The variation of weight-loss with immersion
18 time shows a linear trend, indicating corrosion rate for both microstructures is nearly constant [13].
19 Precipitated microstructure has been heavily attacked by Cl⁻ ions and exhibits an inferior corrosion
20 resistance. The weight loss rate of precipitated microstructure (~ 0.0043 g/cm²) is much higher
21 than that of equiaxed microstructure (~ 0.0012 g/cm²), meaning that precipitated microstructure
22 has poor corrosion resistance. These differences can be attributed to microstructure characteristics,

1 and α_s phase is the preferential dissolution location due to its low content of anodic alloying
2 elements.

3 The immersed surfaces for both microstructures are all initially mirror-like finishes on visual
4 inspection. In the case of immerse in 5 M HCl solution, the entire surface for precipitated
5 microstructure is rapidly darkened due to the preferential corrosion of α_s phase, but the surface of
6 the equiaxed microstructure exhibits no marks of corrosive traces, with only silvery white surface
7 observed. Fig. 9 and Fig. 10 show the SEM images of the detailed surface morphologies for both
8 microstructures after immersed for different time. As the immersion time is not exceeded to 4 days,
9 the uniform corrosion process is observed on both microstructures, and the remarkable selective
10 corrosion is caused by the concentration of Cl^- ions at higher immersion time (longer than 5 days).
11 For the equiaxed microstructure, the corroded surface is covered with evenly distributed corrosion
12 pits and equiaxed β grain. When immersion time is increased to 2 day, the surface has been
13 slightly attacked and a small quantity of corrosion pits is formed on the grain boundaries and grain
14 interiors. The zoomed-in image of a local area for pit morphologies is also inserted in Fig. 9. With
15 the immersion time up to 4 days, only enlarge corrosion pitting is identifiable, and the sizes of pit
16 cavities are increased to approximately 3~8 μm . When the immersion time is increased to 8 days,
17 the sample has been heavily attacked and the entire surface is covered with numerous cusps and
18 cavities with sizes of 10~20 μm . Both grain boundaries and grain interiors are attacked, but more
19 aggressive attack is occurred at grain boundaries. Moreover, localized corrosion occurred on
20 selective grains in the equiaxed microstructure. A large portion of grains and grain boundaries
21 were only slightly attacked.

22 For precipitated microstructure, the remarkably uniform corrosion associated with active

1 dissolution was observed after 2 day immersion (Fig. 10(a)). The surface has been seriously
2 eroded, which is covered with numerous cusps and cavities and exhibits a honeycomb morphology.
3 The preferential area for the aggressive attack is grain boundaries and α_s phases, and the size of
4 the cavities is much larger than 15 μm . The zoomed-in image of the cavities located at grain
5 boundaries and grain interiors is chartered and inserted in Fig. 10. With further increment of
6 immersion time (Fig. 10(b)), the corroded cavities with much larger areas and greater depth are
7 randomly distributed over the surface, indicating precipitated microstructure presents worse
8 corrosion resistance ability. Fig. 10(c) and Fig. 10(d) show the serious surface degradation after 8
9 day and 12 day immersion. The surface undulation is sharply increased and has much higher
10 roughness values. Moreover, the detailed microstructure analysis at the bottom of eroded cavities
11 confirmed that the preferential dissolution locations for precipitated microstructure would be
12 concentrated on α_s phase and $\alpha+\beta$ interphase boundaries. The difference in the composition
13 between α_s and β phase causes the generation of microgalvanic reaction, which result in the
14 preferential corrosion of α_s phase and α/β interphase boundaries.

15 According to the above results, the corrosion rate for precipitated microstructure is much
16 higher than that of equiaxed microstructure, which indicates its weaker corrosion resistance and
17 passive behavior. Fig. 11 shows the schematic diagram of microgalvanic cell formed between
18 acicular α_s and adjacent β phase in the precipitated microstructure. In the initial stage (Fig. 11(a)),
19 the whole surface of precipitated microstructure can rapidly form a continuous passive film, which
20 leads to a rapidly positive shift of the OCP. The conductive circuit has not been formed because of
21 the insulated oxide layer. With elongated immersion time duration (Fig. 11(b)), many corrosive
22 ions (such as Cl^-) will diffuse and accumulate in the film/solution interface from electrolyte

1 solution, and thus the passive film has been heavily attacked. The local breakdown or dissolution
2 of passive film has occurred, which promotes corrosive solution infiltrating into the crevice at
3 film/matrix interface. Moreover, the potential difference (ΔE) between oxide layer and Ti matrix is
4 increased. But because of the effective protection of the passive layer, the galvanic corrosion
5 keeps a steady process and then gradually slows down in this period. At the last stage (Fig. 11(c)),
6 the passive film layer has been completely dissolved and removed, and the substrate is also
7 completely exposed to electrolyte solution, which accelerates the galvanic corrosion between
8 acicular α_s and adjacent β phase. Moreover, ΔE has been increased dramatically, i.e., resulting in
9 an enhancement of driving force for galvanic corrosion. The galvanic current density (I) also
10 increases rapidly and the weight loss is much higher than that in the initial. It is well known that
11 severe pitting corrosion occurs with a large galvanic current density, and thus the effect of
12 metastable pits on the corrosion process cannot be ignored. In this acceleration stage of galvanic
13 corrosion, the nucleation of the pitting in α_s phase and α/β interface can occur at potentials well
14 below the pitting potential, and this nucleation can result in the propagation of the metastable pit.
15 When the pit nucleates at the site, the high reaction rate within the pit will cause a high chloride
16 concentration, which accelerates the galvanic corrosion and enlarge the pit in depth. Therefore, the
17 corrosion mechanism of precipitated microstructures can be explained by the passive behavior,
18 microgalvanic corrosion and pitting.

19 3.4 Mechanical properties degradation

20 Typical engineering stress-strain curves of equiaxed and precipitated microstructures after
21 different immersion times are shown in Fig. 12(a) and Fig. 12(c), and the corresponding
22 mechanical properties are summarized in Fig. 12(b) and Fig. 12(d). Significant difference can be

1 noted in the curves for both types of microstructures after different immersion time. Precipitated
2 microstructure after immersion 14 and 20 days is broken without apparent necking at a very low
3 strain of 0.015, and equiaxed microstructure in different immersion time all show more obvious
4 uniform elongation and necking. When the immersion time is increased to 2 days, ultimate tensile
5 strength (UTS) and elongation (E) of the equiaxed microstructure are 950 MPa and 14.5 %,
6 whereas the precipitated microstructure exhibits a high UTS of 1679 MPa and a low E of 2.8 %.
7 When the immersion time is increased to 20 days, the mechanical properties for both
8 microstructures are all decreases significantly.

9 Based on the above results, it is found that the UTS and E values of both microstructures
10 decrease gradually with the increase of immersion time. Moreover, a much severe degradation of
11 mechanical properties is obtained for precipitated microstructure, implying severe degraded
12 mechanical properties are generated due to the formation of the detrimental microgalvanic cells.
13 The degradation of mechanical properties with increasing immersion time can be mainly attributed
14 to two primary factors. Firstly, many large and deep pitting cavities increase the surface defect,
15 which may act as the crack tip during the deformation. Secondly, hydrogen embrittlement is
16 occurred in the pitting cavities, which is caused by the diffusion of hydrogen ions from the
17 corrosion solution. Therefore, the stability of mechanical properties for Ti-1300 alloy is degraded
18 with the increasing of immersion time, and precipitated microstructure exhibits a more severe
19 mechanical degradation due to nano-scale α_s precipitates.

20 Fig. 13 and Fig. 14 show SEM images of the fracture surfaces for both microstructures
21 ruptured under the immersion time of 8 and 20 days. For the equiaxed microstructure (Fig. 13),
22 the fracture feature is mainly consisted of shear-lip zone at the edge region, as well as the crack

1 propagation zone in the central region. At a higher magnification, the central region exhibits a
2 large number of dimples and cleavage fracture planes surrounded by tearing ridges, and some
3 large and deep equiaxed dimples are present, exhibiting more ductile deformation features. On the
4 contrary, the fracture surface near the edge region consists of the mixture of shallow and parabolic
5 dimples, which belong to shear dimples and form under shear stress in the shear-lip zone (Fig.
6 13(b) and Fig. 13(d)). For equiaxed microstructure, the transgranular fracture and occasional
7 interfacial decohesion between β grains indicate that dimple rupture leads to ductile fracture.
8 When the immersion time is increased to 20 days, the exposed surface has been evidently attacked
9 by the Cl^- ions in the solution, and the shear-lip zone in the outer periphery is smaller than that
10 with immersion time of 8 days. The fracture surface in the crack propagation zone consists of a
11 rugged area surrounded by the ligaments of ductile tearing (Fig. 13(c)), and the outer surface is
12 covered with numerous cusps and cavities with sizes of 10~20 μm located on grain boundaries
13 (Fig. 13(d)).

14 For precipitated microstructure, the fracture feature reveals a mixture feature of cleavage
15 planes and staircase-like morphology, the grain boundary can be also observed (Fig. 14). The
16 fracture occurred preferentially along the prior β grain boundaries, and the cavities are nucleated
17 and propagated at the interface between the prior β grains. This appearance of both coarse and fine
18 boundary facets indicates the enhanced embrittlement, and ultimately leads to poor ductility. In
19 addition, the fracture surfaces show an increase in the fraction of brittle area with increasing
20 immersion time. The fractographs shown in Fig. 14(c) and Fig. 14(d) reveals inter-crystalline
21 fracture and occasional interfacial decohesion between β grains, and that the tearing ridges lie on
22 the individual facets of β grains. The higher magnification shows that the dimples in the shear-lip

zone become slightly larger as the immersion time increases from 8 days to 20 days. This result indicates that the Cl^- concentration significantly affects the cavity nucleation and growth, and these cavities lead to the degraded mechanical properties. Therefore, the absence of mixed features of cleavage planes and staircase indicates the brittle fracture mode for precipitated microstructure, which exhibits the inferior mechanical degradation due to the precipitated α_s phase.

4. Conclusion

(1) In precipitated microstructure, precipitates of α_s phase with an acicular shape around 40 ~ 60 nm in width are distributed inside the β grain, which restricts the growth of other α_s phase due to pinning effect.

(2) Both of equiaxed and precipitated microstructures exhibit spontaneous passivity behavior without obviously active-passive characteristics due to the formation of passive films. XPS results demonstrate that this passive layer is mixed oxides of TiO_2 , Al_2O_3 and Cr_2O_3 .

(3) The α_s precipitates act as the preferential dissolution locations, where “microgalvanic cells” with their adjacent intergranular β phases can be formed to accelerate pitting reaction. The formed microgalvanic cells as well as pitting reactions are identified as the main factor affecting the corrosion performance of Ti-1300 alloy.

(4) The mechanical properties are degraded lineally with immersion time due to pitting reaction. The precipitated microstructure exhibits a much severe mechanical degradation behavior, which is mainly because abundant corrosion cavities are nucleated and propagated at α_s precipitates and prior β grains interface.

Acknowledgments

This work was performed under the support of the Nation Natural Science Foundation of China (Grant No. 51641107 and U1737108) and the Nation Natural Science Foundation of

1 Shaanxi Province (2017JQ5084).

2 **References**

3 [1] A Zafari, Wei XS, Xu W, Xia K. Formation of nanocrystalline β structure in metastable beta Ti
4 alloy during high pressure torsion: The role played by stress induced martensitic transformation.
5 Acta Mater. 97; (2015): 146-155.

6 [2] S Joseph, Lindley TC, Dye D, Saunders EA. The mechanisms of hot salt stress corrosion
7 cracking in titanium alloy Ti-6Al-2Sn-4Zr-6Mo. Corrosion Science. 134; (2018): 169-178.

8 [3] J Ureña, Tsipas S, Pinto AM, Toptan F, Gordo E, Jiménez-Morales A. Corrosion and
9 tribocorrosion behaviour of β -type Ti-Nb and Ti-Mo surfaces designed by diffusion treatments for
10 biomedical applications. Corrosion Science. 140; (2018): 51-60.

11 [4] R Chelariu, Bolat G, Izquierdo J, Mareci D, Gordin DM, Gloriant T, Souto RM. Metastable
12 beta Ti-Nb-Mo alloys with improved corrosion resistance in saline solution. Electrochim. Acta.
13 137; (2014): 280-289.

14 [5] Y Yang, Xia C, Feng Z, Jiang X, Pan B, Zhang X, Ma M, Liu R. Corrosion and passivation of
15 annealed Ti-20Zr-6.5Al-4V alloy. Corros. Sci. 101; (2015): 56-65.

16 [6] X Gai, Bai Y, Li J, Li S, Hou W, Hao Y, Zhang X, Yang R, Misra RDK. Electrochemical
17 behaviour of passive film formed on the surface of Ti-6Al-4V alloys fabricated by electron beam
18 melting. Corrosion Science. 145; (2018): 80-89.

19 [7] A Dalmau, Guiñón PV, Devesa F, Amigó V, Igual MA. Electrochemical behavior of near-beta
20 titanium biomedical alloys in phosphate buffer saline solution. Journal of the Mechanical
21 Behavior of Biomedical Materials. 46; (2015): 59-68.

22 [8] SLD Assis, Wolyneć S, Costa I. Corrosion characterization of titanium alloys by

1 electrochemical techniques. *Electrochim. Acta.* 51; (2006): 1815-1819.

2 [9] S Yan, Song G-L, Li Z, Wang H, Zheng D, Cao F, Horynova M, Dargusch MS, Zhou L. A
3 state-of-the-art review on passivation and biofouling of Ti and its alloys in marine environments. *J.*
4 *Mater. Sci. Technol.* 34; (2018): 421-435.

5 [10] ZB Wang, Hu HX, Zheng YG, Ke W, Qiao YX. Comparison of the corrosion behavior of pure
6 titanium and its alloys in fluoride-containing sulfuric acid. *Corros. Sci.* 103; (2016): 50-65.

7 [11] IM Pohrel'yuk, Fedirko VM, Tkachuk OV, Proskurnyak RV. Corrosion resistance of Ti-6Al-
8 4V alloy with nitride coatings in Ringer's solution. *Corros. Sci.* 66; (2013): 392-398.

9 [12] J Li, Lin X, Guo P, Song M, Huang W. Electrochemical behaviour of laser solid formed Ti-
10 6Al-4V alloy in a highly concentrated NaCl solution. *Corrosion Science.* 142; (2018): 161-174.

11 [13] C Xia, Zhang Z, Feng Z, Pan B, Zhang X, Ma M, Liu R. Effect of zirconium content on the
12 microstructure and corrosion behavior of Ti-6Al-4V- x Zr alloys. *Corros. Sci.* 112; (2016):
13 687-695.

14 [14] J Lu, Zhao Y, Niu H, Zhang Y, Du Y, Wei Z, Huo W. Electrochemical corrosion behavior and
15 elasticity properties of Ti-6Al- x Fe alloys for biomedical applications. *Mat. Sci. Eng., C.* 62;
16 (2016): 36-44.

17 [15] J Li, Li SJ, Hao YL, Huang HH, Bai Y, Hao YQ, Guo Z, Xue JQ, Yang R. Electrochemical
18 and surface analyses of nanostructured Ti-24Nb-4Zr-8Sn alloys in simulated body solution. *Acta*
19 *Biomater.* 10; (2014): 2866-2875.

20 [16] RF Sandenbergh, Lingen EVD. The use of Tafel back extrapolation to clarify the influence of
21 ruthenium and palladium alloying on the corrosion behaviour of titanium in concentrated
22 hydrochloric acid. *Corros. Sci.* 47; (2005): 3300-3311.

- 1 [17] Y Bai, Li SJ, Prima F, Hao YL, Yang R. Electrochemical corrosion behavior of Ti–24Nb–
2 4Zr–8Sn alloy in a simulated physiological environment. *Appl. Surf. Sci.* 258; (2012): 4035-4040.
- 3 [18] Y Bai, Hao YL, Li SJ, Hao YQ, Yang R, Prima F. Corrosion behavior of biomedical
4 Ti-24Nb-4Zr-8Sn alloy in different simulated body solutions. *Materials Science & Engineering C*
5 *Materials for Biological Applications.* 33; (2013): 2159.
- 6 [19] M Nakagawa, Matono Y, Matsuya S, Udoh K, Ishikawa K. The effect of Pt and Pd alloying
7 additions on the corrosion behavior of titanium in fluoride-containing environments. *Biomaterials.*
8 26; (2005): 2239-2246.
- 9 [20] A Biesiekierski, Ping DH, Yamabe-Mitarai Y, Wen C. Impact of ruthenium on microstructure
10 and corrosion behavior of β -type Ti–Nb–Ru alloys for biomedical applications. *Mater. Design.* 59;
11 (2014): 303-309.
- 12 [21] NTC Oliveira, Guastaldi AC. Electrochemical behavior of Ti–Mo alloys applied as
13 biomaterial. *Corros. Sci.* 50; (2008): 938-945.
- 14 [22] TC Niemeyer, Grandini CR, Pinto LMC, Angelo ACD, Schneider SG. Corrosion behavior of
15 Ti–13Nb–13Zr alloy used as a biomaterial. *J. Alloys Compd.* 476; (2009): 172-175.
- 16 [23] J Lu, Ge P, Li Q, Zhang W, Huo W, Hu J, Zhang Y, Zhao Y. Effect of microstructure
17 characteristic on mechanical properties and corrosion behavior of new high strength Ti-1300 beta
18 titanium alloy. *J. Alloys Compd.* 727; (2017):
- 19 [24] I Milošev, Žerjav G, Moreno JMC, Popa M. Electrochemical properties, chemical
20 composition and thickness of passive film formed on novel Ti–20Nb–10Zr–5Ta alloy. *Electrochim.*
21 *Acta.* 99; (2013): 176-189.
- 22 [25] SY Yu, Brodrick CW, Ryan MP, Scully JR. Effects of Nb and Zr Alloying Additions on the

1 Activation Behavior of Ti in Hydrochloric Acid. *J. Electrochem. Soc.* 146; (1999): 4429-4438.

2 [26] KAD Souza, Robin A. Influence of concentration and temperature on the corrosion behavior
3 of titanium, titanium-20 and 40% tantalum alloys and tantalum in sulfuric acid solutions.
4 *Materials Chemistry & Physics.* 103; (2007): 351-360.

5 [27] S Ningshen, Sakairi M, Suzuki K, Okuno T. Corrosion performance and surface analysis of
6 Ti–Ni–Pd–Ru–Cr alloy in nitric acid solution. *Corros. Sci.* 91; (2015): 120-128.

7 [28] D Babilas, Urbańczyk E, Sowa M, Maciej A, Korotin DM, Zhidkov IS, Basiaga M,
8 Krok-Borkowicz M, Szyk-Warszyńska L, Pamuła E. On the electropolishing and anodic oxidation
9 of Ti-15Mo alloy. *Electrochim. Acta.* 205; (2016): 256-265.

10 [29] J Tang, Luo H, Qi Y, Xu P, Lv J, Ma Y, Zhang Z. Effect of nano-scale martensite and β phase
11 on the passive film formation and electrochemical behaviour of Ti-10V-2Fe-3Al alloy in 3.5%
12 NaCl solution. *Electrochimica Acta.* 283; (2018): 1300-1312.

13 [30] H Gerengi, Darowicki K, Bereket G, Slepiski P. Evaluation of corrosion inhibition of
14 brass-118 in artificial seawater by benzotriazole using Dynamic EIS. *Corros. Sci.* 51; (2009):
15 2573-2579.

16 [31] S Fréour, Gloaguen D, François M, Guillén R. Application of inverse models and XRD
17 analysis to the determination of Ti-17 β -phase coefficients of thermal expansion. *Scr. Mater.* 54;
18 (2006): 1475-1478.

19 [32] Y Chen, Li J, Tang B, Kou H, Xue X, Cui Y. Texture evolution and dynamic recrystallization
20 in a beta titanium alloy during hot-rolling process. *J. Alloys Compd.* 618; (2015): 146-152.

21 [33] L Chen, Lin J, Xu X, Li C, Xu Y, Liang Y. Microstructure refinement via martensitic
22 transformation in TiAl alloys. *J. Alloy. Compd.* 741; (2018): 1175-1182.

- 1 [34] Y Huang, Liu Y, Li C, Ma Z, Yu L, Li H. Microstructure evolution and phase transformations
2 in Ti-22Al-25Nb alloys tailored by super-transus solution treatment. *Vacuum*. 161; (2019):
3 209-219.
- 4 [35] Y Li, Xu J. Is niobium more corrosion-resistant than commercially pure titanium in
5 fluoride-containing artificial saliva? *Electrochim. Acta*. 233; (2017): 151-166.
- 6 [36] Y Gui, Zheng ZJ, Gao Y. The bi-layer structure and the higher compactness of a passive film
7 on nanocrystalline 304 stainless steel. *Thin Solid Films*. 599; (2015): 64-71.
- 8 [37] IC Lavosvalereto, Wolyneć S, Ramires I, Guastaldi AC, Costa I. Electrochemical impedance
9 spectroscopy characterization of passive film formed on implant Ti-6Al-7Nb alloy in Hank's
10 solution. *Journal of Materials Science: Materials in Medicine*. 15; (2004): 55-59.
- 11 [38] J Soltis. Passivity breakdown, pit initiation and propagation of pits in metallic materials –
12 Review. *Corros. Sci*. 90; (2015): 5-22.
- 13 [39] JM Macak, Tsuchiya H, Ghicov A, Yasuda K, Hahn R, Bauer S, Schmuki P. TiO₂ nanotubes:
14 Self-organized electrochemical formation, properties and applications. *Curr. Opin. Solid St. M*. 11;
15 (2007): 3-18.
- 16 [40] GT Burstein, Liu C, Souto RM. The effect of temperature on the nucleation of corrosion pits
17 on titanium in Ringer's physiological solution. *Biomaterials*. 26; (2005): 245-256.
- 18 [41] T Balusamy, Kumar S, Narayanan TSNS. Effect of surface nanocrystallization on the
19 corrosion behaviour of AISI 409 stainless steel. *Corros. Sci*. 52; (2010): 3826-3834.
- 20 [42] GV Grigoryan, Grigoryan RP. Electrochemical properties, chemical composition and
21 thickness of passive film formed on novel Ti-20Nb-10Zr-5Ta alloy. *Electrochim. Acta*. 99;
22 (2013): 176-189.

- 1 [43] AWE Hodgson, Mueller Y, Forster D, Virtanen S. Electrochemical characterisation of passive
2 films on Ti alloys under simulated biological conditions. *Electrochim. Acta.* 47; (2002):
3 1913-1923.
- 4 [44] B Hirschorn, Orazem ME, Tribollet B, Vivier V, Frateur I, Musiani M. Determination of
5 effective capacitance and film thickness from constant-phase-element parameters. *Electrochim.*
6 *Acta.* 55; (2010): 6218-6227.
- 7 [45] MA Rodríguez, Carranza RM. Properties of the Passive Film on Alloy 22 in Chloride
8 Solutions Obtained by Electrochemical Impedance. *J. Electrochem. Soc.* 158; (2011): C221-C230.
- 9 [46] GJ Brug, Eeden ALGVD, Sluyters-Rehbach M, Sluyters JH. The analysis of electrode
10 impedances complicated by the presence of a constant phase element. *J. Electroanal. Chem.* 176;
11 (1984): 275-295.
- 12 [47] CH Hsu, Mansfeld F. Technical Note: Concerning the Conversion of the Constant Phase
13 Element Parameter Y_0 into a Capacitance. *Corrosion.* 57; (2001): 747-748.
- 14 [48] IM Pohrelyuk, Fedirko VM, Tkachuk OV, Proskurnyak RV, Proskurnyak RV. Corrosion
15 resistance of Ti-6Al-4V alloy with nitride coatings in Ringer's solution. *Corros. Sci.* 66; (2013):
16 392-398.
- 17 [49] SY Yu, Scully JR, Vitus CM. Influence of Niobium and Zirconium Alloying Additions on the
18 Anodic Dissolution Behavior of Activated Titanium in HCl Solutions. *Inflamm. Bowel. Dis.* 148;
19 (2001): B68-B78.
- 20 [50] JR Rumble, Bickham DM, Powell CJ. The NIST x - ray photoelectron spectroscopy database.
21 <http://srdata.nist.gov/xps>. 7; (2015): 153.
- 22 [51] DD Macdonald, Urquidi - Macdonald M. Theory of Steady - State Passive Films. *J.*

- 1 Electrochem. Soc. 137; (1990): 2395-2402.
- 2 [52] H Krawiec, Vignal V, Loch J, Erasmus-Vignal P. Influence of plastic deformation on the
- 3 microstructure and corrosion behaviour of Ti–10Mo–4Zr and Ti–6Al–4V alloys in the Ringer’s
- 4 solution at 37 °C. Corrosion Science. 96; (2015): 160-170.